A&A, 704, A332 (2025)
https://doi.org/10.1051/0004-6361/202556794

Astronomy & Astrophysics

Distributions and evolution of the equatorial rotation velocities of 2937 BAF-type main-sequence stars from asteroseismology

A break in the specific angular momentum at $M \simeq 2.5\,M_\odot$

Conny Aerts[⋆]

[1] Institute of Astronomy, KU Leuven, Celestijnenlaan 200D, B-3001 Leuven, Belgium
[2] Department of Astrophysics, IMAPP, Radboud University Nijmegen, PO Box 9010, 6500 GL Nijmegen, The Netherlands
[3] Max Planck Institute for Astronomy, Königstuhl 17, 69117 Heidelberg, Germany

Received 8 August 2025 / Accepted 20 October 2025

ABSTRACT

Context. Studies of the rotational velocities of intermediate-mass main-sequence stars are crucial for testing stellar evolution theory. They often rely on spectroscopic measurements of the projected rotation velocities, $V_{\rm eq}\sin i$. These not only suffer from the unknown projection factor $\sin i$ but tend to ignore additional line-profile broadening mechanisms aside from rotation, such as pulsations and turbulent motions near the stellar surface. This limits the accuracy of $V_{\rm eq}$ distributions derived from $V_{\rm eq}\sin i$ measurements.
Aims. We use asteroseismic measurements to investigate the distribution of the equatorial rotation velocity $V_{\rm eq}$, its ratio with respect to the critical rotation velocity, $V_{\rm eq}/V_{\rm crit}$, and the specific angular momentum, J/M, for several thousands of BAF-type stars, covering a mass range from 1.3 $M_\odot$ to 8.8 $M_\odot$ and almost the entire core-hydrogen burning phase.
Methods. We rely on high-precision model-independent internal rotation frequencies, as well as on masses and radii from asteroseismology to deduce $V_{\rm eq}$, $V_{\rm eq}/V_{\rm crit}$, and J/M for 2937 gravity-mode pulsators in the Milky Way. The sample stars have rotation frequencies between almost zero and 33 μHz, corresponding to rotation periods above 0.35 d.
Results. We find that intermediate-mass stars experience a break in their J/M occurring in the mass interval $[2.3, 2.7]\,M_\odot$. We establish unimodal $V_{\rm eq}$ and $V_{\rm eq}/v_{\rm crit}$ distributions for the mass range $[1.3, 2.5]\,M_\odot$, while stars with $M \in [2.5, 8.8]\,M_\odot$ reveal some structure in their distributions. We find that the near-core rotation slows down as stars evolve, pointing to very efficient angular momentum transport.
Conclusions. The kernel density estimators of the asteroseismic internal rotation frequency, equatorial rotation velocity, and specific angular momentum of this large sample of intermediate-mass field stars can conveniently be used for population synthesis studies and to fine-tune the theory of stellar rotation across the main sequence evolution.

Key words. asteroseismology – stars: evolution – stars: interiors – stars: magnetic field – stars: oscillations – stars: rotation

1. Introduction

Single low-mass stars rotate at a pace far below their critical velocity, $V_{\rm crit}$, defined as the velocity for which the outwards centrifugal force at the star's equator overcomes the inward force of gravity in a co-rotating frame of reference. In this work we follow Aerts et al. (2019) and define low-mass stars as having a birth mass, M, below 1.3 times the mass of the Sun ($M < 1.3\,M_\odot$). All these single stars experience a so-called Kraft break (Kraft 1967). This break is caused by angular momentum loss due to a magnetised wind, which is fed by a dynamo in the convective envelope. Although high-precision space photometry revealed the magnetic braking to stall somewhat during the second half of the main sequence (van Saders et al. 2016; Hall et al. 2021; Metcalfe et al. 2022), the rotational spin-down is very effective due to the magnetic activity of the star, particularly in the early stages after birth (Kawaler 1988).

The effective spin-down of low-mass stars caused by the magnetised wind gives rise to the practical age-dating tool of gyrochronology, originally introduced by Skumanich (1972) and further refined by many studies since then (e.g. Barnes 2003). Age-dating from gyrochronology via measurement of the surface rotation period got a major upgrade since modern high-precision uninterrupted space photometric light curves became available (e.g. Barnes 2010; Meibom et al. 2015), particularly when cross-calibrated by independent methods such as modelling of young open clusters (e.g. the series of papers by Fritzewski et al. 2020, 2021, 2023, 2024b).

In terms of the range in stellar mass, the Kraft break is quite sharp: it becomes ineffective when crossing a narrow mass range of ∼0.1 $M_\odot$ wide (Beyer & White 2024), separating the slowly rotating low-mass stars from the intermediate-mass stars. Again following Aerts et al. (2019), we define intermediate-mass stars as having a mass in the range $1.3\,M_\odot < M < 8\,M_\odot$. This split up between the two groups of stars agrees well with the physical distinction caused by the Kraft break occurring in the mass range $[1.3, 1.4]\,M_\odot$ (Beyer & White 2024). We do point out that Beyer & White (2024) deleted young field stars from their sample, while these stars' higher $v\sin i$ might be due to them being of intermediate mass rather than of low mass and young age. In this sense, the Kraft break could still be somewhat more gradual when larger samples of field stars are being considered.

Intermediate-mass stars reveal a broad range of observed rotation velocities, from hardly any rotation up to their critical velocity. This broad coverage occurs because magnetic braking

⋆ Corresponding author: conny.aerts@kuleuven.be

is ineffective or absent as these stars have only a thin convective envelope or none at all. The disappearance of the thin convective envelope and effective spin-down in intermediate-mass stars is not known to be as sharp in terms of the stellar mass as the classical Kraft break. Rather, the change in behaviour of the rotational velocities and angular momenta were found to occur between roughly $M \simeq 1.5\,M_\odot$ and $M \simeq 2.5\,M_\odot$, depending on the metallicity, the internal rotation at birth, and the angular momentum loss (Kawaler 1988).

From measured projected rotation velocities, $V_{\rm eq} \sin i$, for stars with spectral type between B0 and F9.5 by Fukuda (1982), and assuming a random distribution of the inclination angle between the rotation axis and the line-of-sight, Kawaler (1987) found the specific angular momentum, J/M, of dwarfs to depend on mass as $J/M \propto M^{1.09}$ when excluding Be and Am stars, as we will do in this work. Since that seminal paper, numerous observational studies with spectroscopic $V_{\rm eq} \sin i$ measurements for large samples of field stars were undertaken (e.g. Royer et al. 2007; Abt 2009; Huang et al. 2010, to list just a few).

Spectroscopic measurements are readily available from large surveys and are often considered to deduce the rotation periods of intermediate-mass stars. Such stars experience diverse variable phenomena, notably large-scale oscillations (see the samples by Balona et al. 2011; Balona 2013; Balona et al. 2015; Van Reeth et al. 2015b; Pápics et al. 2017; Bowman & Kurtz 2018; Antoci et al. 2019; Li et al. 2020; Szewczuk et al. 2021; Kurtz 2022, the latter providing a thorough overview). The variability caused by the multiperiodic oscillations is often dominant over rotational modulation caused by spots in photometric light curves. This makes the derivation of the surface rotation periods from such data much harder than for low-mass stars, where the rotational modulation caused by the magnetic activity dominates the photometric variability.

In this study we shed new light on stellar rotation from asteroseismic measurements of the cyclic near-core rotation frequency, denoted here as $f_{\rm rot}$, and of the accompanying equatorial rotation velocity, $V_{\rm eq}$, for almost 3000 field stars covering the mass range $M \in [1.3, 8.8]\,M_\odot$. This includes stars having thin convective shells in their otherwise radiative outer envelope due to partial ionisation of helium or iron-like isotopes, which occur at temperatures of $\simeq$40 kK and $\simeq$200 kK, respectively. These ionisation layers cause large-scale low-degree oscillation modes excited by the opacity mechanism (Pamyatnykh 1999) or by flux blocking (Guzik et al. 2000; Dupret et al. 2005). Turbulent pressure may also occur in the envelope and may additionally cause small-scale high-degree oscillations (Grassitelli et al. 2015, 2016). This gives rise to a rather complex envelope structure. Due to their thin convective envelope, intermediate-mass stars are found to be incapable of creating or sustaining an effective magnetic dynamo as their low-mass analogues can. Hence they keep their initial rotation velocity throughout most of their main-sequence phase and only slow down appreciably as of their hydrogen shell burning phase (Huang et al. 2010; Zorec & Royer 2012; Aerts et al. 2019; Aerts 2021).

Our aims are to provide distributions and to study the evolution of the internal rotation frequency and the equatorial rotation velocity of intermediate-mass stars, without having to rely on uncertain spectroscopic $V_{\rm eq} \sin i$ estimates. Rather, we use asteroseismology of gravity-mode pulsators in the Milky Way. These field stars occur along the main sequence in the Hertzsprung-Russell diagram from the bottom of the instability strip of the γ Doradus (γ Dor hereafter) stars (Dupret et al. 2005, $M > 1.2\,M_\odot$) all the way into the strip of the slowly pulsating B (SPB) stars (Szewczuk & Daszyńska-Daszkiewicz 2017; Pedersen et al. 2020, $M < 9\,M_\odot$). Modern space data revealed these pulsators to cover the entire main sequence in terms of evolutionary stage, without any interruption in mass, as highlighted by Gaia Collaboration (2023), Aerts et al. (2023), Hey & Aerts (2024), Mombarg et al. (2024). They are hence a suitable population to calibrate the theory of stellar rotation and angular momentum for the intermediate-mass regime.

2. The two asteroseismic samples

We considered isolated intermediate-mass stars in the Milky Way occurring mostly above the Kraft break, although some of them have a mass between 1.3 $M_\odot$ and 1.4 $M_\odot$ and thus might be subject to classical spin down. Two substantial samples of gravity-mode pulsators having their fundamental parameters determined from asteroseismic grid modelling are available in the literature. All the pulsators in these two samples have prograde dipole oscillation modes identified from *Kepler* or Transiting Exoplanet Survey Satellite (TESS) high-precision photometric light curves. This space photometry led to a measurement of their internal rotation frequency in the transition layer between the convective core and radiative envelope following the methods by Van Reeth et al. (2015a, 2016) and Aerts et al. (2025a). This measurement of $f_{\rm rot}$ is deduced from period spacing patterns of identified modes and relies on the computation of the eigenvalues of Laplace's Tidal Equations (Townsend 2020) following the Traditional Approximation of Rotation (Townsend 2003; Mathis 2013). This method assumes rigid rotation as well as modes with a large spin parameter, $s \equiv 2f_{\rm rot}/f_{\rm corot}$ with the denominator being the mode frequency in a frame of reference corotating with the star. These assumptions are well fulfilled for the high-order gravity modes in intermediate-mass pulsators (Van Reeth et al. 2016; Li et al. 2020; Aerts et al. 2021), making the measurements of $f_{\rm rot}$ independent of stellar models. The mass (M expressed in $M_\odot$), radius (R expressed in $R_\odot$), and evolutionary stage (defined as the ratio of the current hydrogen mass fraction in the fully mixed convective core to the initial value, $X_{\rm c}/X_{\rm ini}$) of the pulsators were deduced in a homogeneous way from a grid of rotating stellar models calibrated by asteroseismology and computed by Mombarg et al. (2024). These models have a fixed initial metallicity $Z = 0.014$. Further, the grid considers rotation rates between 5% and 55% of the critical rate and covers the mass range $[1.3, 9.0]\,M_\odot$. It includes core boundary mixing by adopting an exponentially decaying convective core overshooting with its efficiency described by a free parameter. Rotational mixing in the envelope is also included in the models, but without any free parameters by relying on the theory by Zahn (1992) and Chaboyer & Zahn (1992).

While the asteroseismic modelling strategy was similar, these two samples were selected from different criteria:

1. The first sample (Sample 1 hereafter) consists of 490 γ Dor pulsators modelled by Fritzewski et al. (2024a). We use their inferred masses, radii, and evolutionary stages from grid modelling relying on four input observables. The first three are the ten-base logarithm of the effective temperature ($\log(T_{\rm eff})$) and luminosity ($\log(L/L_\odot)$) from *Gaia* data release (DR) 3, and the measured asteroseismic asymptotic period spacing Π_0 (see Aerts et al. 2010, for a definition). This seismic observable was deduced from *Kepler* space photometry by Li et al. (2020), who relied on prograde gravity or gravito-inertial modes of consecutive radial order following the method developed by Van Reeth et al. (2015a, 2016). Aside from Π_0, Li et al. (2020) also measured the stars' near-core rotation frequency, $f_{\rm rot}$, from identified

prograde modes. This fourth observable comes with superb precision, often better than 1%, irrespective of the used methodology (Ouazzani et al. 2019, Fig. 5). This sample covers $f_{\rm rot} \in [0, 33]\mu$Hz.

2. The second sample (Sample 2) is composed of 2464 gravito-inertial prograde dipole mode pulsators distilled by Aerts et al. (2025a) from combined *Gaia* and TESS photometric light curves. For these stars, the dominant mode was used to estimate $f_{\rm rot}$ from the recipe designed by Aerts et al. (2025a). This regression formula is only valid for gravito-inertial modes in moderate and not too fast rotators (in the definition by Aerts & Tkachenko (2024), which we adopt here) having a mode spin parameter $s > 1$. Hence, by construction, this sample does not contain the slowest nor the fastest rotators among intermediate-mass pulsators. In practice, it covers $f_{\rm rot} \in [3, 28]\mu$Hz. The masses, radii, and evolutionary stages of these 2464 pulsators were determined from the same stellar model grid used for Sample 1. However, in this case these parameters were inferred from the *Gaia* DR3 $\log(T_{\rm eff})$ and $\log(L/L_\odot)$, and from $f_{\rm rot}$ as the three observables, because there is no asteroseismic measurement of Π_0 available for these stars.

As an update for Aerts (2021, their Fig. 6), we show the measured near-core rotation frequency as a function of the model-dependent gravity deduced from the masses and radii in Fig. 1. The figure also contains a comparison of these quantities for our sample stars with those of more than a thousand red giants from mixed dipole modes detected in *Kepler* observations. Figure 1 visualises the difference in selection criteria for our two samples, where Aerts et al. (2025a) restricted to pulsators having a dominant gravito-inertial mode with spin value $s > 1$. We also point to a lack of stars with a rotation frequency around 6.5 μHz. This is an artefact of the exclusion of stars having a dominant frequency of exactly once per day, which may be an intrinsic oscillation mode but could also be due to an instrumental alias frequency rather than being a stellar signal (cf. Hey & Aerts 2024). Vetting such objects implies an underrepresentation of stars with $f_{\rm rot} \simeq 6.5\,\mu$Hz after application of the recipe in Aerts et al. (2025a, Eq. (4)). This is particularly visible for stars towards the end of the main sequence.

Figure 1 illustrates the spin-down of the near-core rotation during the main sequence and towards the red giant phase for evolved stars with a mass below $\simeq 2.5\,M_\odot$. Rather than using $\log g$ to indicate how far the stars are evolved along the main sequence, we will work with the evolutionary stage $X_{\rm c}/X_{\rm ini}$, which decreases from one at the zero-age main sequence (ZAMS) to zero at the terminal-age main sequence (TAMS). This proxy for the evolutionary stage is a more useful quantity for the broad mass range covered by Samples 1 and 2, irrespective of the actual stellar age. Moreover, $X_{\rm c}/X_{\rm ini}$ is well accessible by asteroseismic modelling based on low-frequency gravity modes because these probe the region adjacent to the convective core (Pedersen et al. 2018, 2021; Mombarg et al. 2021; Michielsen et al. 2021).

Eight stars belong to both samples. Their masses and radii are in agreement to within 1σ and differ less than $0.061\,M_\odot$ and $0.235\,R_\odot$, respectively. For these stars, we took the results for $f_{\rm rot}$ from Li et al. (2020) because this measurement relies on tens of modes rather than just the dominant one and is therefore more precise than the one following the recipe from Aerts et al. (2025a) – see Fig. 1 for typical errors. We thus keep these stars in Sample 1 and delete them from Sample 2. Moreover, nine of the stars in Aerts et al. (2025a) turn out to have a too imprecise mass, radius, or $f_{\rm rot}$ because their values would make them rotate faster than the critical Keplerian rotation velocity, $V_{\rm crit}$ (Aerts et al. 2025b). We therefore excluded these nine stars from Sample 2, ending up with a total of 2447 gravito-inertial pulsators from Aerts et al. (2025a). This gives us a total number of 2937 pulsators to work with in the following sections. The median errors for the asteroseismic masses and radii in Sample 1 amount to $0.139\,M_\odot$ and $0.116\,R_\odot$, respectively. For Sample 2 these median errors are $0.049\,M_\odot$ and $0.138\,R_\odot$[1].

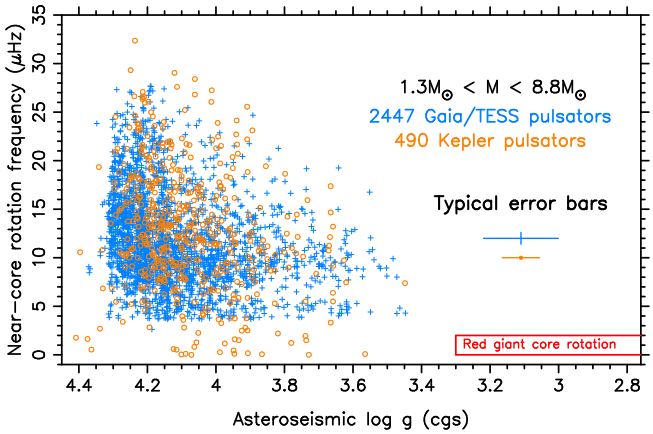

Fig. 1. Near-core rotation frequency $f_{\rm rot}$ versus asteroseismic gravity for two samples: 490 *Kepler* gravity- and gravito-inertial mode pulsators with prograde modes from Fritzewski et al. (2024a, orange circles) and 2447 gravito-inertial prograde dipole mode pulsators from Aerts et al. (2025a, blue crosses). The position of the same quantities for more than a thousand red giant stars from mixed-mode asteroseismology is indicated by the red rectangle produced from Aerts et al. (2019, Fig. 4).

3. Equatorial rotation velocities and specific angular momenta

Stellar rotation studies in the literature covering similarly large samples of field stars in the galaxy as ours measured $V_{\rm eq} \sin i$ from spectral line broadening. These measurements thus have, by construction, infinite uncertainty due to the unknown inclination angle. This is usually corrected for by making the reasonable assumption that the inclination angles are randomly oriented to deduce $V_{\rm eq}$ as $2/\pi \cdot (V_{\rm eq} \sin i)$ (Abt 2001).

Relying on various data sources, the landmark study by Zorec & Royer (2012) assembled $V_{\rm eq} \sin i$ measurements for a sample of 2014 B6- to F2-type stars in the galaxy, covering the mass range $[1.4, 5.2]\,M_\odot$. They assumed a 10% relative error for their assembled $V_{\rm eq} \sin i$ measurements, which is rather optimistic given that many of the intermediate-mass main-sequence stars are also subject to time-dependent spectral line broadening mechanisms, such as oscillations, spots, or turbulent envelope convection, to list just a few (Aerts et al. 2009; Grassitelli et al. 2015; Frémat et al. 2023; Aerts et al. 2023). When these phenomena are ignored in the derivation of $V_{\rm eq} \sin i$, the values are systematically overestimated (Aerts et al. 2014).

Zorec & Royer (2012) performed their study prior to the space asteroseismology revolution. The latter meanwhile showed that the theory of angular momentum transport adopted in stellar models relying on the local conservation of angular momentum needs appreciable fixes for stars of low and intermediate mass. This was derived from observed dipole gravity or

[1] For reasons of reproducibility and follow-up studies, the used stellar parameters for the 2937 stars are provided in electronic form in Tables 1 and 2 at the CDS.

mixed modes, which offer the best probing power of the deep interiors of stars and allow for optimal calibration of stellar evolution theory (Mosser et al. 2014; Aerts et al. 2019; Fuller et al. 2019; Eggenberger et al. 2022; Moyano et al. 2023).

With our Samples 1 and 2, we offer a complementary study to the one by Zorec & Royer (2012), keeping in mind the recent asteroseismic insights into stellar rotation and angular momentum transport. Thanks to the observed properties of identified dipole modes, our measurements of the rotation come straight from the stellar interior, where the evolution of stars is directed. Moreover, as the median values of the errors for the masses and radii quoted at the end of the previous section illustrate, these fundamental parameters from grid modelling based on dipole-mode asteroseismology come with much smaller errors than those resulting from evolutionary tracks in the Hertzsprung-Russell diagram as adopted by Zorec & Royer (2012, typically an order of magnitude better, see their Table 2).

Rather than relying on spectroscopic $V_{\rm eq}\sin i$ measurements, we computed the asteroseismic equatorial rotation velocity, $V_{\rm eq} \equiv 2\pi \cdot f_{\rm rot} \cdot R$ for the 2937 stars in our two samples, from the model-independent measurement of $f_{\rm rot}$ and an asteroseismically inferred radius. We did so while assuming rigid rotation to make our study compatible with the results from modern asteroseismology. Van Reeth et al. (2018) and Li et al. (2020) have indeed shown that F-type stars are quasi-rigid rotators during the entire main sequence, as the near-core and surface rotation frequencies of tens of single γ Dor stars differ less than 10% (see Fig. 6 in Aerts 2021, for a summary plot). More massive B- or A-type pulsators may reveal a systematically higher level of differential rotation between the core and envelope, or between the envelope and surface. Ratios of the near-core or envelope rotation and the surface rotation have values typically between one and two for carefully done case studies on individual pulsators (Briquet et al. 2007; Dziembowski & Pamyatnykh 2008; Suárez et al. 2009; Kurtz et al. 2014; Saio et al. 2015; Triana et al. 2015; Salmon et al. 2022; Vanlaer et al. 2025). A homogeneous ensemble study with constraints on the internal rotation from space-based asteroseismology is available for stars at the high-mass end of our second sample. It concerns tens of field β Cep stars observed with TESS and *Gaia*. This revealed almost all of them to have envelope-to-surface rotation rates below two as well (Fritzewski et al. 2025b). All of these asteroseismology studies imply that quasi-rigid rotation is a valid approach for our two treated samples of main-sequence stars. We come back to this assumption in Sect. 4.

The second factor of uncertainty for $V_{\rm eq}$ is connected with the modelled radius for our two samples. From Fritzewski et al. (2024a) and Mombarg et al. (2024), this has an estimated relative uncertainty of roughly 10% for the adopted input physics of the stellar model grid. Overall this means that the computed asteroseismic $V_{\rm eq}$ values have similar uncertainty than the spectroscopic studies, but are built on measurements from the stellar interior rather than the surface (Aerts 2021), and rely on rotating stellar models that are compatible with asteroseismic measurements.

We computed Kernel Density Estimates (KDEs) for the near-core rotation frequency $f_{\rm rot}$, the equatorial surface velocity $V_{\rm eq}$, the ratio of $V_{\rm eq}$ and the critical Keplerian rotation velocity $V_{\rm crit} \equiv \sqrt{G\,M/R^3}$, and the specific angular momentum $J/M = 2/3 \cdot (2\pi \cdot f_{\rm rot}) \cdot R^2$ with the `statsmodels` library of routines (Seabold & Perktold 2010) available in the `python` software package `numpy` (Harris et al. 2020). These KDEs were calculated assuming a normal distribution and by relying on Scott's rule (Scott 1979) to deduce the optimal bandwidth. This rule gave equivalent results to Silverman's approach (Silverman 1986) for bandwidth estimation. Normalised histograms were subsequently constructed for each of the four distributions, adopting the optimal bandwidths. These histograms for the two samples are shown in Fig. 2, along with the KDEs. We find the stars in Sample 1, which consists only of early F-type stars, to rotate somewhat faster than the much larger Sample 2 composed of BAF-type stars.

By construction Sample 1 offers broader distributions, because Sample 2 does not contain the slowest rotators nor covers the tail towards the highest rotation frequencies that do occur in Sample 1 (cf. Fig. 1). We performed non-parametric two-sided Kolmogorov-Smirnoff (KS) tests with the `stats` modules of the software package SciPy (Virtanen et al. 2020) to evaluate the null hypothesis of dealing with identical underlying continuous distributions for the two samples. The resulting $p-$values amounted to $1.9\cdot10^{-5}$ for $f_{\rm rot}$, $1.3\cdot10^{-5}$ for $V_{\rm eq}$, 10^{-9} for $V_{\rm eq}/V_{\rm crit}$, and $1.5 \cdot 10^{-9}$ for J/M. The four null hypotheses were thus rejected with high levels of confidence ($p < 0.0001$) such that, for all four quantities, the underlying distributions from Samples 1 and 2 indeed differ from each other on formal statistical grounds, in line with their astrophysical selection criteria discussed in Sect. 2.

Even if some structure occurs in the panels of Fig. 2, we find essentially unimodal distributions for the four quantities. This stands in contrast to the results by Zorec & Royer (2012, their Fig. 6), who claimed bimodal distributions from their sample when dividing it into six sub-samples with overlaping mass intervals. This bimodality persisted when redistributing stars of mass between 2.4 $M_\odot$ and 3.85 $M_\odot$ according to three evolutionary stages deduced from stellar models (their Fig. 9). However, the bimodality disappeared and turned into a unimodal distribution for the stars with mass between 1.6 $M_\odot$ and 2.4 $M_\odot$. Rather than relying on a model age, we consider the evolutionary stage as inferred from asteroseismic modelling and study the specific angular momentum properties of the samples in the next Section.

4. A break in the specific angular momentum

We now return to the concept of the Kraft break in low-mass stars, causing their surface rotational spin-down due to the magnetic dynamo created in the convective envelope. It is generally understood that their angular momentum loss is due to a magnetised wind but models of the internal structure encompassing the angular momentum transport and loss remain uncertain (Sarkar et al. 2024) and the transition region between early and late F-type stars is poorly understood (Santos et al. 2025). As already mentioned in the introduction, intermediate-mass stars cannot create and sustain a large-scale magnetic dynamo as their convective envelope is either too thin or their envelope is dominantly radiative.

Our two samples contain a few F-type stars in the transition region of the Kraft break but almost all of them have a mass above 1.4 $M_\odot$. Figure 1 reveals their spin-down of the region adjacent to the convective core as the stellar evolution progresses. This points to the evacuation of the local angular momentum away from the transition layer between the convective core and radiative envelope. We now evaluate how J/M depends on the stellar mass and evolutionary stage, assuming that the stars keep their rotation to be quasi-rigid, as was found for F-type pulsators by Li et al. (2020).

Following Kawaler (1987, Fig. 2) we plot the logarithm of J/M versus M in the upper panel of Fig. 3 for the two samples studied here, along with those for two small additional samples

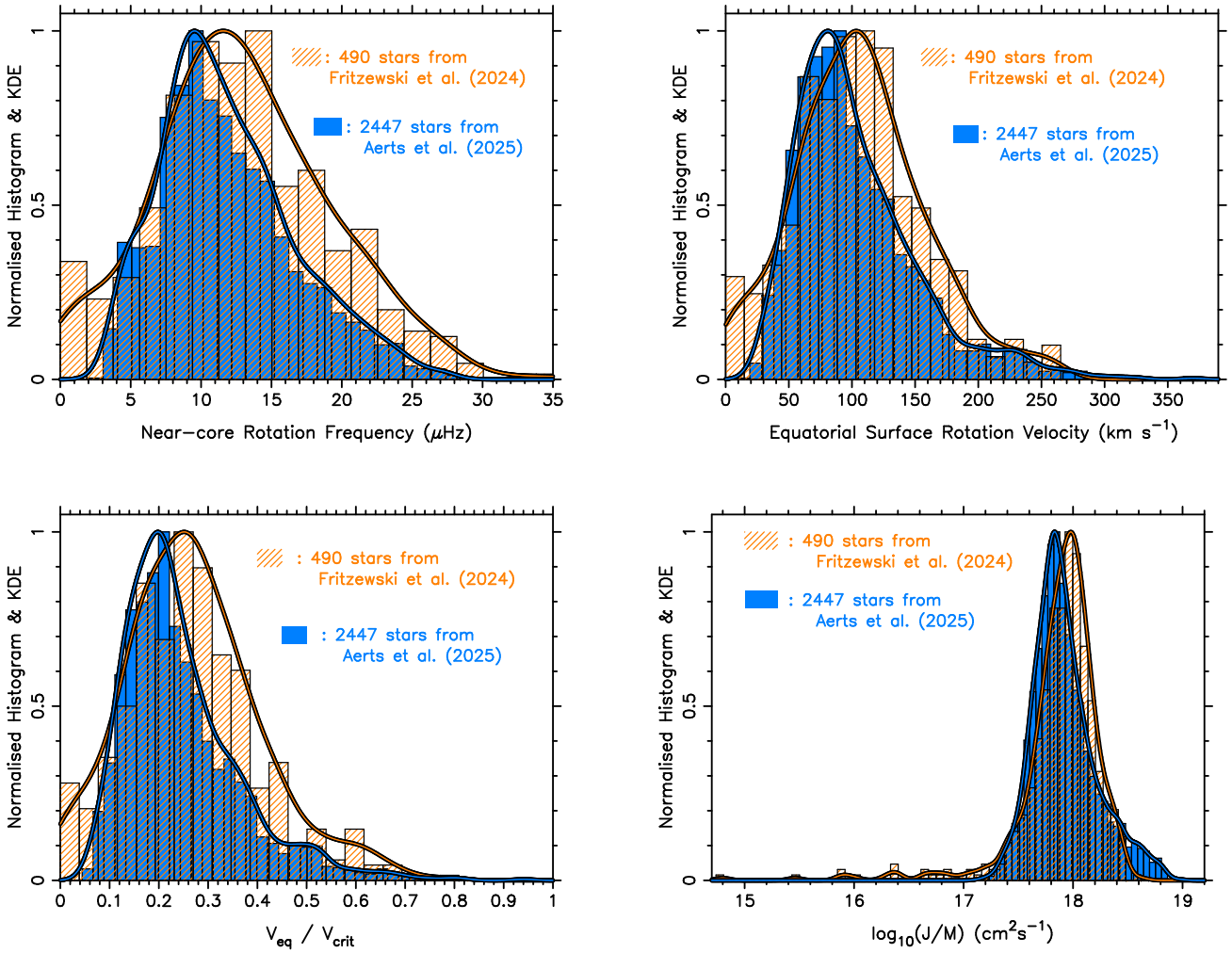

Fig. 2. Kernel density estimates (full lines) and histograms constructed with optimal bandwidth for Sample 1 (orange hatched) and Sample 2 (blue). Upper left: model-independent measurement of $f_{\rm rot}$; upper right: model-dependent $V_{\rm eq}$; lower left: model-dependent $V_{\rm eq}/V_{\rm crit}$; lower right: model dependent specific angular momentum J/M.

of SPB and γ Dor stars with the best asteroseismic modelling to date. The forward modelling for these 58 stars is based on the fitting of tens of individual identified gravity-mode frequencies per star, delivering the size and mass of their convective core aside from their global mass and radius. For these 58 stars we can therefore also plot the spectific angular momentum of their convective core. A first result from Fig. 3 is that the total J/M of these 58 pulsators is in good agreement with the one for our two large samples whose modelling is based on global observables rather than fitting of individual mode frequencies. It can also be seen that J/M of the convective core is typically two to three orders of magnitude smaller than the one of the entire star.

We further indicate the two measured upper limits for J/M in the top panel of Fig. 3, one for each sample. The orange (Sample 1) and blue (Sample 2) straight lines result from the two stars with the highest measured J/M value. To make these lines somewhat independent of the choice of one particular star, we indicate in grey the region covered by the upper limits when considering several different pairs of stars among those with the highest J/M values for each of the two samples. We find a break in the upper limits of the measured J/M at about $2.5\pm0.2\,{\rm M}_\odot$. This break occurs in the range $[2.3, 2.7]\,{\rm M}_\odot$ and is thus a different one than the Kraft break in the mass range $[1.3, 1.4]\,{\rm M}_\odot$ reported by Beyer & White (2024, see the two vertical dashed lines), separating the slowly rotating low-mass stars from the entire population of the intermediate-mass stars. Kraft (1967) considered $2\,{\rm M}_\odot$ as a cutoff in mass above which a different steepening of the $J-M$ relation occurs. Our large asteroseismic samples reveal a break in the specific angular momentum at $M \simeq 2.5\,{\rm M}_\odot$, sub-dividing the intermediate-mass stars into those that still have a thin convective outer envelope and those with a pure radiative envelope aside from some thin convective shells due to partial ionisation zones with increased opacity (Pamyatnykh 1999, Figs. 1 and 2).

The upper limits given by the two lines in Fig. 3 represent the relationships $J \propto M^{2.48}$ for $M \leq 2.5\,{\rm M}_\odot$ and $J \propto M^{1.50}$ for $M > 2.5\,{\rm M}_\odot$. We thus recover a steepening of the specific angular momentum for stars with a mass below the transition range $[2.3, 2.7]\,{\rm M}_\odot$. In comparison, Kraft (1970) found $J \propto M^{1.6}$ considering stars with spectral type earlier than F0, picking this cutoff in spectral type rather arbitrarily. By relying on stellar models with rigid rotation – in retrospect a highly modern approach proven justified by space asteroseismology – Kawaler (1987) deduced $J \propto M^{2.1}$ for stars with spectral types from B0 to F9.5, excluding Ap and Be stars as is the case for our two samples. We have now sharpened these old limits and clarified the value of the cutoff mass from our much bigger samples with asteroseismically inferred J/M values.

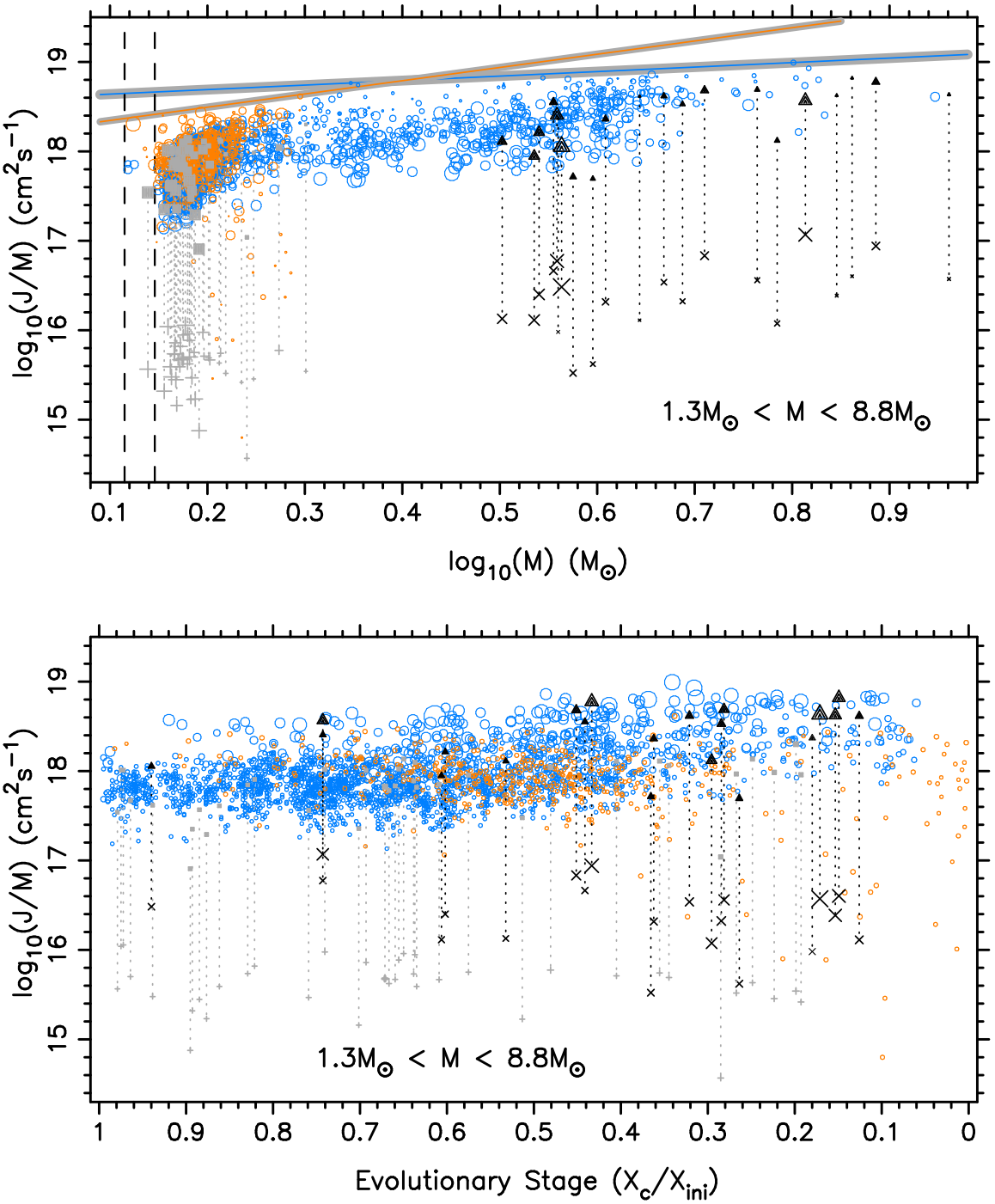

Fig. 3. Specific angular momentum, J/M, plotted logarithmically against stellar mass (upper panel) and evolutionary stage (lower panel). The symbol size for each star scales linearly with its evolutionary stage X_c/X_{ini} (upper panel) and mass (lower panel). The circles show the stars of Samples 1 and 2. Also shown are the J/M values of 21 SPB stars from Pedersen (2022a,b triangles, from her Tables 4 and 5), connected by a dotted line to the specific angular momentum of their convective core deduced from asteroseismic modelling of individual identified modes (shown as ×). Similarly, J/M of the 37 asteroseismically modelled γ Dor stars from Mombarg et al. (2021) are shown as filled squares connected to the specific angular momentum of their convective core (shown as +). The two dashed vertical lines in the upper panel indicate the mass regime $[1.3, 1.4]\,M_\odot$ where the Kraft break occurs. The two coloured full lines and their uncertainty regions (in grey) denote the upper limits of the J/M measurements for each of the two samples.

In terms of evolutionary stage (lower panel of Fig. 3), we find that J/M hardly changes or decreases for most stars with a mass below the transition region of $[2.3, 2.7]\,M_\odot$. We note that several stars in Sample 1 are outliers in terms of lower J/M values (see also the tail towards lower values in the lower right panel of Fig. 2). Most of these stars occur during the second part of the main sequence and could be merger products or stripped stars resulting from interacting binaries. Further we notice that many of the stars in Sample 2 with a mass above the transition region of $[2.3, 2.7]\,M_\odot$ show an increasing trend in J/M. Since stars lose angular momentum unless they accrete matter, the lower panel of Fig. 3 suggests that our assumption of rigid rotation in a single

star may not be appropriate for all the stars in this mass regime. The trend in J/M for this sub-population of Sample 2 is in line with the measurements of internal rotation for early B stars. Such pulsators so far revealed internal-to-surface rotation frequencies up to a factor two (Vanlaer et al. 2025; Fritzewski et al. 2025b). Such an internal-to-surface rotation ratio would imply a shift of value 0.3 downwards in $\log_{10}(J/M)$ in Fig. 3.

In order to assess the evolutionary change of J/M further, we redistributed all the stars in the two samples into five sub-samples according to their inferred X_c/X_{ini}. We show the histograms and KDEs of the near-core rotation frequency and the specific angular momentum for the sub-samples in these five evolutionary stages in Fig. 4, where the y-axes in the upper panels show the actual numbers per bin of evolutionary stage and the lower panels the corresponding normalised KDEs. The left panels of this figure show that the measured near-core rotation slows down during the main sequence evolution, as also illustrated in Fig. 1. This implies efficient angular momentum transport away from the transition layer between the convective core and radiative envelope, as already concluded by Aerts et al. (2019) from smaller asteroseismic samples and from Sample 2 by Aerts et al. (2025a). This is nowadays understood in terms of the joint effects of (magneto-)hydrodynamical processes occurring during the stars' evolution (e.g. Pedersen 2022a; Mombarg 2023; Moyano et al. 2023, 2024). The seismic measurements of the near-core rotation of intermediate-mass stars stand in sharp contrast with the spin up of the cores of such stars based on local conservation of angular momentum as was still assumed in the stellar evolution models used by Zorec & Royer (2012). The lower left panel shows that a bimodal distribution pops up for the stars that approach the TAMS. This sub-sample (in purple) consists of only 58 stars and the bimodality is caused by the artefact already discussed in the context of Fig. 1. It is due to stars with $f_{rot} \simeq 6.5\,\mu$Hz being under-represented in Sample 2, particularly in the later stage of the main sequence.

The right panels of Fig. 4 illustrate that the overestimation of J/M due to our assumption of rigid rotation occurs mainly for $X_c/X_{ini} < 0.4$. The lower right panel of this figure, along with the bottom panel of Fig. 3 point out that stars with a mass above the transition range $[2.3, 2.7]\,M_\odot$ develop differential rotation up to a factor two to three (corresponding to a shift of 0.3 and 0.5 downwards in $\log_{10}(J/M)$, respectively) as they move towards the TAMS during the second half of the main sequence.

Given the break in J/M at $M \simeq 2.5\,M_\odot$, and the homogeneous treatment of the two samples in terms of grid modelling, it makes sense to re-arrange them in terms of their asteroseismic mass and redetermine the distributions of V_{eq} and V_{eq}/V_{crit}. We show histograms and KDEs when we group the stars according to a mass below or above $2.5\,M_\odot$ in Fig. 5. We observe that stars in the lower mass bin rotate slower in absolute terms and also with respect to their critical rate than those in the higher mass bin. The lower and higher mass populations peak at rotation velocities near 20% and 30% of the critical velocity, respectively.

In line with Zorec & Royer (2012), who dealt with smaller sample sizes in their spectroscopic $V_{eq} \sin i$ study, we find that the stars with mass above $2.5\,M_\odot$ have a somewhat more complex distribution of their equatorial rotation velocity compared to the unimodal smooth distribution of the lower mass stars. As shown in Fig. 3, the stars with $M < 2.5\,M_\odot$ are characterised by a steeper J versus M relationship, pointing to a stronger spin-down mechanism active in their interior.

From our two mass bins, we find hints of a dip around $V_{eq} = 170\,\mathrm{km\,s^{-1}}$ along with an extra hump between $V_{eq} = 200\,\mathrm{km\,s^{-1}}$ and $V_{eq} = 250\,\mathrm{km\,s^{-1}}$, although this structure levels off when considering V_{eq}/V_{crit}. We checked that this dip is unrelated to the lower density of stars with $f_{rot} \simeq 6.5\,\mu$Hz in Fig. 1 as all the stars in this V_{eq} range have a higher rotation frequency. This small hump may simply be due to the smaller size of the asteroseismic sample with stars having $M > 2.5\,M_\odot$, also reflected in the larger optimal bandwidth for that sample ($20.6\,\mathrm{km\,s^{-1}}$ versus $8.6\,\mathrm{km\,s^{-1}}$ for the stars with $M < 2.5\,M_\odot$). Zorec & Royer (2012) did not find such a hump at this rotational velocity but the sample they used for the construction of the KDEs does not include stars with $M \geq 4\,M_\odot$ while we have 117/377 stars in that mass regime.

5. Discussion and conclusions

Thanks to the *Kepler* and TESS space missions, gravity and gravito-inertial asteroseismology of intermediate-mass main-sequence stars is now a mature field of research (Aerts & Tkachenko 2024). This opens new doors for the calibration of stellar evolution models and for population synthesis studies based on high-precision rotational properties from asteroseismology. We have explored the two homogeneously analysed samples of intermediate-mass pulsators with identified dipole gravity modes. The distributions of their rotational equatorial velocity and specific angular momentum were determined. Our overall sample consists of 2937 pulsators covering almost the entire main sequence. This allowed us to unravel how the distribution of J/M evolves during core-hydrogen burning.

Guided by the asteroseismic result that the near-core rotation frequency – a model-independent measurement – decreases as the stars evolve along the main sequence, we derived a break in the $(M, J/M)$ relationship. Stars with a mass below the transition region of $[2.3, 2.7]\,M_\odot$ have a steeper relation than the more massive stars. This transition region coincides roughly with the (dis)appearance of a convective envelope for stars with sun-like metallicity. This points towards a more effective evacuation of angular momentum when a thin rotating convective envelope is present compared to the case where it is absent. In their review, Rempel et al. (2023) conclude that small-scale dynamo fields are expected to be active across the Hertzsprung-Russell diagram in all stars with an outer convective zone. The authors stress that self-consistently generated small-scale fields are only beginning to be understood and being simulated for real circumstances. Their simulations for an F dwarf reveal small-scale dynamo activity, which has an impact on the structure of the star just below the surface. Such small-scale fields and the instabilities they cause may be in operation in stars with $M < 2.5\,M_\odot$ and may be feeding a thin magnetised wind, while being absent in stars with $M > 2.5\,M_\odot$. Also, from magneto-hydrodynamical simulations of rotating convection, Bekki (2025) finds that small-scale dynamo fields have a non-negligible impact on angular momentum transport in the rotating convective envelopes of stars.

From detected gravito-inertial modes, γ Dor pulsators are predicted to have stronger internal magnetic fields compared to SPB stars (Aerts et al. 2021, their Fig. 8). Considering that 3D simulations of core convection in rotating A-type stars cause an effective magnetic dynamo in action (Brun et al. 2005), the stronger internal fields in AF-type stars may cause more effective angular momentum transport from the innermost regions to the envelope layers than in B stars. These internal and envelope magnetic properties acting together may imply an overall more efficient angular momentum transport and loss for stars in the mass regime [1.3,2.5] $M_\odot$ than for stars with higher masses. We

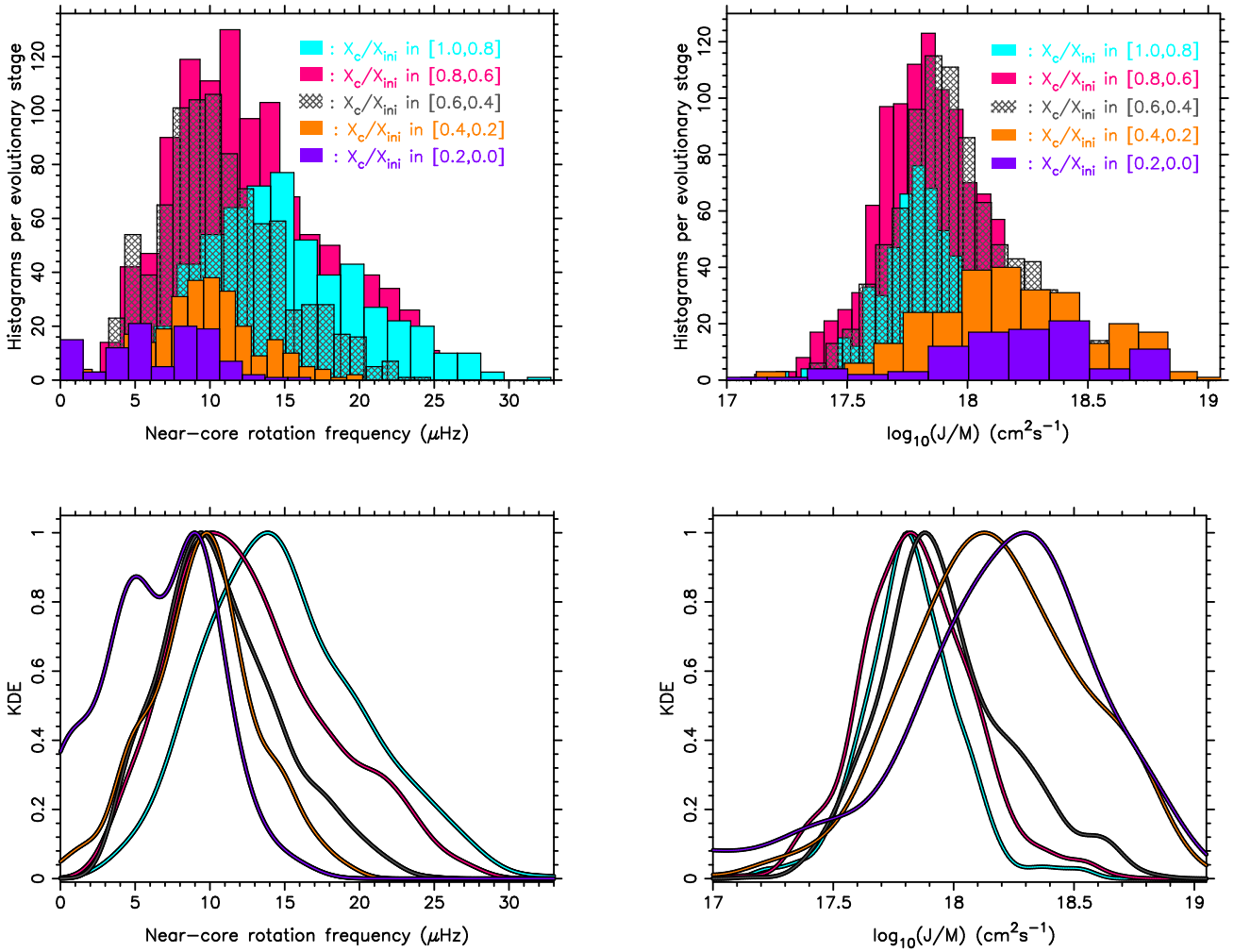

Fig. 4. Histograms (upper panels) and KDEs (lower panels) of the near-core rotation frequency (left) and specific angular momentum (right), where the two samples are considered jointly, split up into five regimes of evolutionary stage from near-ZAMS (cyan) to near-TAMS (purple).

also found hints that stars with $M > 2.5\,M_\odot$ deviate from rigid rotation as they approach the TAMS. Both phenomena may point to different internal magnetic properties below and above the break we found. This hypothesis on the role of large-scale internal and small-scale envelope dynamo fields in the presence of rotation needs to be tested further from dedicated 3D magneto-hydrodynamical simulations covering the entire star instead of only particular regions as is usually done for computational convenience. From the observational side, asteroseismic modelling applied to gravity modes including the Lorentz force in the presence of fast rotation as developed by Rui et al. (2024) can shed new light on the properties of the internal magnetic fields, which were so far often neglected in the asteroseismic forward modelling of intermediate-mass stars.

While our study offers alternative KDEs based on higher precision asteroseismic measurements and inferred stellar parameters compared to those in the spectroscopic study by Zorec & Royer (2012), it still has room for improvements. First, the two asteroseismic samples consist of intermediate-mass stars with sun-like metallicity while the properties of convection depend on this parameter. Moreover, just as the Zorec & Royer (2012) study, our two samples are limited to field stars in the galaxy, and therefore do not cover rotation at the stellar birth on the ZAMS and the earliest initial phases of stellar evolution very close to the ZAMS when the stars are still in their birth cluster. The number of stars near the TAMS is limited, and we do not have any stars confirmed to be in the fast contraction phase of the main sequence approaching core-hydrogen exhaustion on a thermal time scale (stars in 'the hook'). Stellar cores do spin up in this rapid phase of evolution, as is known from the extended main sequence turnoff stars in young open clusters (e.g. Bastian et al. 2018). While spectroscopic studies of $V_{\rm eq}\sin i$ of the youngest (say, less than 300 Myr) open clusters are numerous (e.g. Dufton et al. 2019; Kamann et al. 2023; Cristofari et al. 2025, to list just a few recent ones) and point to fast rotating populations being the cause of split main sequences, our sample of field stars does not cover the earliest evolutionary phases and is limited in the coverage of the fastest rotators. This is due to the selection function of our two samples being composed of pulsators with identified dipole gravity modes. Asteroseismology of young open clusters with ages below 300 Myr recently got kickstarted (Bedding et al. 2023; Fritzewski et al. 2024b, 2025a; Li et al. 2024, 2025) and will be intensified in the near future with the prolonged TESS mission and the PLATO mission on the horizon (Rauer et al. 2025). Early studies already revealed that several clusters have fast rotators with prograde dipole modes in their TESS data. Such asteroseismic studies of young clusters will be of great help to extend our two samples towards the youngest and fastest rotating intermediate-mass stars and those close to exhausting their central hydrogen.

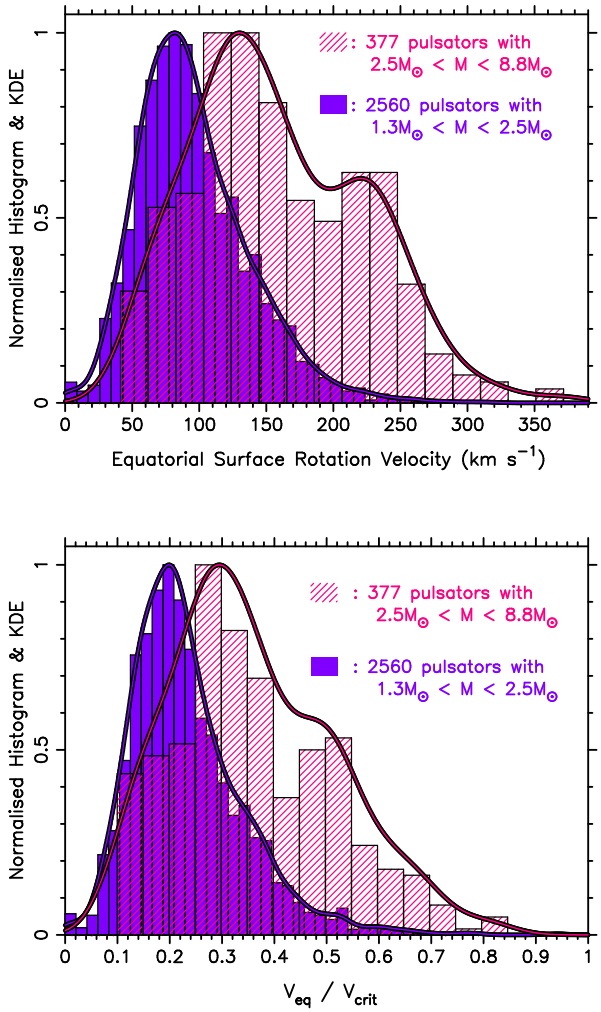

Fig. 5. Kernel density estimates (full lines) and histograms constructed with optimal bandwidth for the stars split up according to masses below or above 2.5 $M_\odot$. Upper panel: $V_{\rm eq}$; lower panel: $V_{\rm eq}/V_{\rm crit}$.

Data availability

Tables 1 and 2 with the parameters of the 2937 stars are available at the CDS via https://cdsarc.cds.unistra.fr/viz-bin/cat/J/A+A/704/A332

Acknowledgements. The author is grateful to Mathijs Vanrespaille, Dario Fritzewski, Saskia Hekker, and the anonymous referee for valuable comments that helped to improve the paper. The research leading to these results has received funding from the European Research Council (ERC) under the Horizon Europe programme (Synergy Grant agreement N°101071505: 4D-STAR). While partially funded by the European Union, views and opinions expressed are however those of the author only and do not necessarily reflect those of the European Union or the European Research Council. Neither the European Union nor the granting authority can be held responsible for them.

References

Abt, H. A. 2001, AJ, 122, 2008
Abt, H. A. 2009, AJ, 138, 28
Aerts, C. 2021, Rev. Mod. Phys., 93, 015001
Aerts, C., & Tkachenko, A. 2024, A&A, 692, R1
Aerts, C., Puls, J., Godart, M., & Dupret, M. A. 2009, A&A, 508, 409
Aerts, C., Christensen-Dalsgaard, J., & Kurtz, D. W. 2010, Asteroseismology (Heidelberg: Springer-Verlag)
Aerts, C., Simón-Díaz, S., Groot, P. J., & Degroote, P. 2014, A&A, 569, A118
Aerts, C., Mathis, S., & Rogers, T. M. 2019, ARA&A, 57, 35
Aerts, C., Augustson, K., Mathis, S., et al. 2021, A&A, 656, A121
Aerts, C., Molenberghs, G., & De Ridder, J. 2023, A&A, 672, A183
Aerts, C., Van Reeth, T., Mombarg, J. S. G., & Hey, D. 2025a, A&A, 695, A214
Aerts, C., Van Reeth, T., Mombarg, J. S. G., & Hey, D. 2025b, A&A, 698, C3
Antoci, V., Cunha, M. S., Bowman, D. M., et al. 2019, MNRAS, 490, 4040
Balona, L. A. 2013, MNRAS, 431, 2240
Balona, L. A., Pigulski, A., De Cat, P., et al. 2011, MNRAS, 413, 2403
Balona, L. A., Daszyńska-Daszkiewicz, J., & Pamyatnykh, A. A. 2015, MNRAS, 452, 3073
Barnes, S. A. 2003, ApJ, 586, 464
Barnes, S. A. 2010, ApJ, 722, 222
Bastian, N., Kamann, S., Cabrera-Ziri, I., et al. 2018, MNRAS, 480, 3739
Bedding, T. R., Murphy, S. J., Crawford, C., et al. 2023, ApJ, 946, L10
Bekki, Y. 2025, A&A, in press, http://dx.doi.org/10.1051/0004-6361/202556923
Beyer, A. C., & White, R. J. 2024, ApJ, 973, 28
Bowman, D. M., & Kurtz, D. W. 2018, MNRAS, 476, 3169
Briquet, M., Morel, T., Thoul, A., et al. 2007, MNRAS, 381, 1482
Brun, A. S., Browning, M. K., & Toomre, J. 2005, ApJ, 629, 461
Chaboyer, B., & Zahn, J. P. 1992, A&A, 253, 173
Cristofari, P. I., Dupree, A. K., Milone, A. P., Mateo, M., & Chiarpotti, M. 2025, ApJ, in press, [arXiv:2508.02599]
Dufton, P. L., Evans, C. J., Hunter, I., Lennon, D. J., & Schneider, F. R. N. 2019, A&A, 626, A50
Dupret, M. A., Grigahcène, A., Garrido, R., Gabriel, M., & Scuflaire, R. 2005, A&A, 435, 927
Dziembowski, W. A., & Pamyatnykh, A. A. 2008, MNRAS, 385, 2061
Eggenberger, P., Moyano, F. D., & den Hartogh, J. W. 2022, A&A, 664, L16
Frémat, Y., Royer, F., Marchal, O., et al. 2023, A&A, 674, A8
Fritzewski, D. J., Barnes, S. A., James, D. J., & Strassmeier, K. G. 2020, A&A, 641, A51
Fritzewski, D. J., Barnes, S. A., James, D. J., & Strassmeier, K. G. 2021, A&A, 652, A60
Fritzewski, D. J., Barnes, S. A., Weingrill, J., et al. 2023, A&A, 674, A152
Fritzewski, D. J., Aerts, C., Mombarg, J. S. G., Gossage, S., & Van Reeth, T. 2024a, A&A, 684, A112
Fritzewski, D. J., Van Reeth, T., Aerts, C., et al. 2024b, A&A, 681, A13
Fritzewski, D. J., Kemp, A., Li, G., & Aerts, C. 2025a, A&A, submitted
Fritzewski, D. J., Vanrespaille, M., Aerts, C., et al. 2025b, A&A, 698, A253
Fukuda, I. 1982, PASP, 94, 271
Fuller, J., Piro, A. L., & Jermyn, A. S. 2019, MNRAS, 485, 3661
Gaia Collaboration (De Ridder, J., et al.) 2023, A&A, 674, A36
Grassitelli, L., Fossati, L., Langer, N., et al. 2015, A&A, 584, L2
Grassitelli, L., Fossati, L., Langer, N., et al. 2016, A&A, 593, A14
Guzik, J. A., Kaye, A. B., Bradley, P. A., Cox, A. N., & Neuforge, C. 2000, ApJ, 542, L57
Hall, O. J., Davies, G. R., van Saders, J., et al. 2021, Nat. Astron., 5, 707
Harris, C. R., Millman, K. J., van der Walt, S. J., et al. 2020, Nature, 585, 357
Hey, D., & Aerts, C. 2024, A&A, 688, A93
Huang, W., Gies, D. R., & McSwain, M. V. 2010, ApJ, 722, 605
Kamann, S., Saracino, S., Bastian, N., et al. 2023, MNRAS, 518, 1505
Kawaler, S. D. 1987, PASP, 99, 1322
Kawaler, S. D. 1988, ApJ, 333, 236
Kraft, R. P. 1967, ApJ, 150, 551
Kraft, R. P. 1970, in Spectroscopic Astrophysics. An Assessment of the Contributions of Otto Struve, eds. G. H. Herbig, & O. Struve, 385
Kurtz, D. W. 2022, ARA&A, 60, 31
Kurtz, D. W., Saio, H., Takata, M., et al. 2014, MNRAS, 444, 102
Li, G., Van Reeth, T., Bedding, T. R., et al. 2020, MNRAS, 491, 3586
Li, G., Aerts, C., Bedding, T. R., et al. 2024, A&A, 686, A142
Li, G., Mombarg, J. S. G., Guo, Z., & Aerts, C. 2025, A&A, 703, A116
Mathis, S. 2013, in Lecture Notes in Physics, eds. M. Goupil, K. Belkacem, C. Neiner, F. Lignières, & J. J. Green (Berlin: Springer Verlag), 865, 23
Meibom, S., Barnes, S. A., Platais, I., et al. 2015, Nature, 517, 589
Metcalfe, T. S., Finley, A. J., Kochukhov, O., et al. 2022, ApJ, 933, L17
Michielsen, M., Aerts, C., & Bowman, D. M. 2021, A&A, 650, A175
Mombarg, J. S. G. 2023, A&A, 677, A63
Mombarg, J. S. G., Van Reeth, T., & Aerts, C. 2021, A&A, 650, A58
Mombarg, J. S. G., Aerts, C., Van Reeth, T., & Hey, D. 2024, A&A, 691, A131
Mosser, B., Benomar, O., Belkacem, K., et al. 2014, A&A, 572, L5
Moyano, F. D., Eggenberger, P., Salmon, S. J. A. J., Mombarg, J. S. G., & Ekström, S. 2023, A&A, 677, A6
Moyano, F. D., Eggenberger, P., & Salmon, S. J. A. J. 2024, A&A, 681, L16
Ouazzani, R. M., Marques, J. P., Goupil, M. J., et al. 2019, A&A, 626, A121
Pamyatnykh, A. A. 1999, Acta Astron., 49, 119
Pápics, P. I., Tkachenko, A., Van Reeth, T., et al. 2017, A&A, 598, A74
Pedersen, M. G. 2022a, ApJ, 940, 49

Pedersen, M. G. 2022b, ApJ, 930, 94
Pedersen, M. G., Aerts, C., Pápics, P. I., & Rogers, T. M. 2018, A&A, 614, A128
Pedersen, M. G., Escorza, A., Pápics, P. I., & Aerts, C. 2020, MNRAS, 495, 2738
Pedersen, M. G., Aerts, C., Pápics, P. I., et al. 2021, Nat. Astron., 5, 715
Rauer, H., Aerts, C., Cabrera, J., et al. 2025, Exp. Astron., 59, 26
Rempel, M., Bhatia, T., Bellot Rubio, L., & Korpi-Lagg, M. J. 2023, Space Sci. Rev., 219, 36
Royer, F., Zorec, J., & Gómez, A. E. 2007, A&A, 463, 671
Rui, N. Z., Ong, J. M. J., & Mathis, S. 2024, MNRAS, 527, 6346
Saio, H., Kurtz, D. W., Takata, M., et al. 2015, MNRAS, 447, 3264
Salmon, S. J. A. J., Moyano, F. D., Eggenberger, P., Haemmerlé, L., & Buldgen, G. 2022, A&A, 664, L1
Santos, A. R. G., Godoy-Rivera, D., Mathur, S., et al. 2025, A&A, 697, A177
Sarkar, A., Eggenberger, P., Yungelson, L., & Tout, C. A. 2024, MNRAS, 532, 3441
Scott, D. W. 1979, Biometrika, 66, 605
Seabold, S., & Perktold, J. 2010, in 9th Python in Science Conference
Silverman, B. W. 1986, Density Estimation for Statistics and Data Analysis (London, New York: Chapman & Hall)
Skumanich, A. 1972, ApJ, 171, 565
Suárez, J. C., Moya, A., Amado, P. J., et al. 2009, ApJ, 690, 1401
Szewczuk, W., & Daszyńska-Daszkiewicz, J. 2017, MNRAS, 469, 13
Szewczuk, W., Walczak, P., & Daszyńska-Daszkiewicz, J. 2021, MNRAS, 503, 5894
Townsend, R. H. D. 2003, MNRAS, 340, 1020
Townsend, R. H. D. 2020, MNRAS, 497, 2670
Triana, S. A., Moravveji, E., Pápics, P. I., et al. 2015, ApJ, 810, 16
Van Reeth, T., Tkachenko, A., Aerts, C., et al. 2015a, A&A, 574, A17
Van Reeth, T., Tkachenko, A., Aerts, C., et al. 2015b, ApJS, 218, 27
Van Reeth, T., Tkachenko, A., & Aerts, C. 2016, A&A, 593, A120
Van Reeth, T., Mombarg, J. S. G., Mathis, S., et al. 2018, A&A, 618, A24
van Saders, J. L., Ceillier, T., Metcalfe, T. S., et al. 2016, Nature, 529, 181
Vanlaer, V., Bowman, D. M., Burssens, S., et al. 2025, A&A, 701, A5
Virtanen, P., Gommers, R., Oliphant, T. E., et al. 2020, Nat. Methods, 17, 261
Zahn, J. P. 1992, A&A, 265, 115
Zorec, J., & Royer, F. 2012, A&A, 537, A120